PHYSICAL REVIEW B, VOLUME 64, 134422

Langevin simulation of thermally activated magnetization reversal in nanoscale pillars

Gregory Brown,[1] M. A. Novotny,[1] and Per Arne Rikvold[1,2]
[1]*School of Computational Science and Information Technology, Florida State University, Tallahassee, Florida 32306-4120*
[2]*Center for Materials Research and Technology and Department of Physics, Florida State University, Tallahassee, Florida 32306-4350*

(Received 31 January 2001; revised manuscript received 10 April 2001; published 13 September 2001)

Numerical solutions of the Landau-Lifshitz-Gilbert micromagnetic model incorporating thermal fluctuations and dipole-dipole interactions (calculated by the fast multipole method) are presented for systems composed of nanoscale iron pillars of dimension 9 nm×9 nm×150 nm. Hysteresis loops generated under sinusoidally varying fields are obtained, while the coercive field is estimated to be 1979 ± 14 Oe using linear field sweeps at $T=0$ K. Thermal effects are essential to the relaxation of magnetization trapped in a metastable orientation, such as happens after a rapid reversal of an external magnetic field less than the coercive value. The distribution of switching times is compared to a simple analytic theory that describes reversal with nucleation at the ends of the nanomagnets. Results are also presented for arrays of nanomagnets oriented perpendicular to a flat substrate. Even at a separation of 300 nm, where the field from neighboring pillars is only ~ 1 Oe, the interactions have a significant effect on the switching of the magnets.

DOI: 10.1103/PhysRevB.64.134422 PACS number(s): 75.75.+a, 65.80.+n, 61.46.+w, 64.60.Qb

I. INTRODUCTION

Several emerging technologies will incorporate fabricated magnets that are small enough to contain only a single magnetic domain. These nanoscale magnets will be essential for smaller components, lower power consumption, and completely new applications in fields such as information storage, integrated circuits, sensor technology, and microelectromechanical systems. Successful implementation of these technologies requires a fundamental understanding of the dynamics of the internal magnetic structure of the nanoscale magnets on time scales ranging from the nanoseconds associated with gigahertz applications to the years over which magnetic information storage must be stable.

An essential factor in many of these applications, especially in information storage, is the free-energy barrier that separates two antiparallel orientations of the magnetization. This free-energy barrier can be surmounted using thermal energy momentarily "borrowed" from the surroundings, and often device engineers strive for barriers of at least $40k_{\mathrm{B}}T$ to make this thermal bit-flipping a rare event. Here T is the absolute temperature and k_{B} is Boltzman's constant. The particle can be magnetized in a specified direction by applying a field strong enough to remove the free-energy barrier. The smallest field sufficient to do this at zero temperature is called the coercive field H_{c}. Fields smaller than the coercive field cannot change the magnetization orientation deterministically, but they do cause lower free-energy barriers and make thermal crossing more probable. In fact, hybrid recording[1] uses lower-than-coercive fields and thermal barrier crossing to write data in high-coercivity magnetic media.

Two examples of particular thermally activated barrier crossings are shown in Fig. 1. Red is associated with the magnetization orientation antiparallel to the applied field, which is metastable. Blue is associated with the parallel magnetization, which is thermodynamically stable. Green and yellow are intermediate between the two orientations. For times before those shown in the figure, the magnet stays in the metastable state with end caps of nonuniform magnetization induced by pole avoidance. Eventually thermal fluctuations in the end caps carry the system over the free-energy barrier. After the barrier crossing, the entire magnet changes quickly to the stable equilibrium orientation.

Often, nanoscale magnets are assumed to be uniformly magnetized bodies. For instance, Garcìa-Palacios and Lázaro[2] considered the stochastic trajectories of isolated magnetic moments using the Landau-Lifshitz-Gilbert equation subject only to applied fields and a uniaxial anisotropy, which supplied the free-energy barrier. They measured the susceptibility of the magnetization in small sinusoidal probe fields. Multiple crossing of the free-energy barrier, a frequently noted consequence of the gyromagnetic motion in single-spin models, was also observed for their uniform-magnetization model.

When at least one dimension of the nanomagnet is greater than the exchange length of the material, nonuniform reversal modes become energetically possible. To consider such nonuniform magnetization reversal we use micromagnetic simulation with a large number of points inside the magnet. Specifically, nanomagnets with an aspect ratio of approximately 17 are considered throughout this work and are referred to as pillars. The numerical approach is discussed in Sec. II, with further details found in the appendixes. Results for the estimation of the coercive field and the statistics of magnetization switching are discussed in Sec. III. A simple model for nonuniform switching is discussed in Sec. IV. Section V considers the effect of interactions between pillars in a one-dimensional array. A brief summary of the results is given in Sec. VI. Some preliminary results of this study were presented in Refs. 3–5.

II. NUMERICAL DETAILS

The basic approach of micromagnetic modeling is to consider a system of coarse-grained magnetization vectors $\tilde{\mathbf{M}}(\tilde{\mathbf{r}}_i)$, with $\tilde{\mathbf{r}}_i$ indicating the location in space of the ith spin. The vectors are assumed to have a fixed magnitude M_s, corresponding to the bulk saturation magnetization density of

©2001 The American Physical Society

TABLE I. Parameters used in the micromagnetic simulations described here.

l_e	3.6 nm
M_s	1700 emu/cm^3
$\Delta\tilde{\mathbf{r}}$	1.5 nm
$\Delta\tilde{t}$	5.0×10^{-5} ns
γ_0	1.76×10^{7} Hz/Oe
α	0.1

the material. This is a valid approximation for temperatures well below the Curie temperature.[6] The evolution of each magnetization vector is governed by the damped precessional motion given by the Landau-Lifshitz-Gilbert (LLG) equation[7,8]

$$\frac{d\tilde{\mathbf{M}}(\tilde{\mathbf{r}}_i)}{d\tilde{t}}=\frac{\gamma_0}{1+\alpha^2}\tilde{\mathbf{M}}(\tilde{\mathbf{r}}_i)\times\left(\tilde{\mathbf{H}}(\tilde{\mathbf{r}}_i)-\frac{\alpha}{M_s}\tilde{\mathbf{M}}(\tilde{\mathbf{r}}_i)\times\tilde{\mathbf{H}}(\tilde{\mathbf{r}}_i)\right), \tag{1}$$

where the electron gyromagnetic ratio is $\gamma_0=1.76\times10^7$ Hz/Oe,[8] and α is a phenomenological damping parameter. For the sign of the undamped-precession term we follow the convention of Brown.[7] Here a tilde is used to distinguish dimensional quantities from their dimensionless counterparts, which will be introduced later.

The dynamics are controlled by $\tilde{\mathbf{H}}(\tilde{\mathbf{r}}_i)$, the local field at the ith position, which, in general, is different at each lattice site. The local field mediates all of the interactions in the system with the contributions combined via linear superposition,

$$\tilde{\mathbf{H}}(\tilde{\mathbf{r}}_i)=\tilde{\mathbf{H}}_{\rm z}(\tilde{\mathbf{r}}_i)+\tilde{\mathbf{H}}_{\rm e}(\tilde{\mathbf{r}}_i)+\tilde{\mathbf{H}}_{\rm d}(\tilde{\mathbf{r}}_i)+\tilde{\mathbf{H}}_{\rm a}(\tilde{\mathbf{r}}_i)+\tilde{\mathbf{H}}_{\rm n}(\tilde{\mathbf{r}}_i), \tag{2}$$

where $\tilde{\mathbf{H}}_{\rm z}(\tilde{\mathbf{r}}_i)$ represents the externally applied field (Zeeman term), $\tilde{\mathbf{H}}_{\rm e}(\tilde{\mathbf{r}}_i)$ is due to exchange effects, $\tilde{\mathbf{H}}_{\rm d}(\tilde{\mathbf{r}}_i)$ is the dipole field, $\tilde{\mathbf{H}}_{\rm a}(\tilde{\mathbf{r}}_i)$ is due to crystalline anisotropy, and $\tilde{\mathbf{H}}_{\rm n}(\tilde{\mathbf{r}}_i)$ is the random field induced by thermal noise.[9] The estimates used for each of these fields are given below, except for $\tilde{\mathbf{H}}_{\rm a}(\tilde{\mathbf{r}}_i)$, which we have taken to be zero. In this article, a tilde emphasizes that the symbol represents a quantity with units; the corresponding dimensionless quantity is written without the tilde. Material parameters, such as M_s, always have units when appropriate.

We have chosen material parameters to match those of bulk iron; a summary of all parameters used here is given in Table I. The saturation magnetization density is $M_s=1700$ emu/cm^3,[10] while the exchange length, the length over which $\tilde{\mathbf{M}}$ can change appreciably, is $l_{\rm e}=3.6$ nm.[11,12] The damping parameter α has proved difficult to measure or estimate from *ab initio* considerations, and may even depend on numeric details.[13] Here we have chosen $\alpha=0.1$ to represent the underdamped behavior usually assumed to exist in nanoscale magnets. In the other extreme, the overdamped limit, the gyromagnetic motion intrinsic to the LLG equation is suppressed, and the system can be more efficiently simulated using Monte Carlo methods.[14,15]

The magnetization was discretized on a cubic lattice with discretization length $\Delta\tilde{r}=1.5$ nm chosen to give sufficient resolution across the cross section of the pillar. The time discretization of $\Delta\tilde{t}=5\times10^{-14}$ s was chosen to avoid numerical instabilities in the integration. The details of the integration scheme are given below. The equation of motion was cast into dimensionless quantities by considering the rescaled length $\mathbf{r}=\tilde{\mathbf{r}}/l_{\rm e}$, time $t=\gamma_0 M_s\tilde{t}$, field $\mathbf{H}=\tilde{\mathbf{H}}/M_s$, and magnetization density $\mathbf{M}=\tilde{\mathbf{M}}/M_s$. This rescaling is facilitated in cgs units,[10] where magnetic fields can be normalized by the magnetization density without the inclusion of any constants.

In a continuum model, exchange represents local differences in the alignment of the magnetization. The contribution to the local field from exchange interactions can be approximated by $l_{\rm e}^2\nabla^2\tilde{\mathbf{M}}(\tilde{\mathbf{r}})$,[8] which has been implemented in the simulations by

$$\tilde{\mathbf{H}}_{\rm e}(\tilde{\mathbf{r}}_i)=\left(\frac{l_{\rm e}}{\Delta\tilde{r}}\right)^2\left(-6\tilde{\mathbf{M}}(\tilde{\mathbf{r}}_i)+\sum_{|\tilde{\mathbf{d}}|=\Delta\tilde{r}}\tilde{\mathbf{M}}(\tilde{\mathbf{r}}_i+\tilde{\mathbf{d}})\right), \tag{3}$$

where the summation is over the six nearest neighbors of $\tilde{\mathbf{r}}_i$. Here the exchange length is defined in terms of the exchange energy[16] $E_{\rm e}=-(l_e^2/2)\int d\mathbf{r}\tilde{\mathbf{M}}\cdot\nabla^2\tilde{\mathbf{M}}$. The dimensionless form of the exchange contribution to the local field is

$$\mathbf{H}_{\rm e}(\mathbf{r}_i)=\left(\frac{1}{\Delta r}\right)^2\left(-6\mathbf{M}(\mathbf{r}_i)+\sum_{|\mathbf{d}|=\Delta r}\mathbf{M}(\mathbf{r}_i+\mathbf{d})\right). \tag{4}$$

The computationally most intensive part of determining the local field is finding the contribution from dipole-dipole interactions, $\mathbf{H}_{\rm d}(\mathbf{r})$. Efficient calculation, which uses the fast multipole method (FMM),[17] is quite involved and is discussed in Appendix A.

Thermal fluctuations are included in the LLG equation of motion by inclusion in the superposition of a random field $\tilde{\mathbf{H}}_{\rm n}(\tilde{\mathbf{r}})$ with Gaussian fluctuations whose first moments are zero and whose second moments obey the fluctuation-dissipation relation[9]

$$\langle\tilde{H}_{{\rm n}\mu}(\tilde{\mathbf{r}}_i,\tilde{t})\tilde{H}_{{\rm n}\mu'}(\tilde{\mathbf{r}}_i',\tilde{t}')\rangle=\frac{2\alpha k_{\rm B}T}{\gamma_0 M_s V}\,\delta(\tilde{t}-\tilde{t}')\,\delta_{\mu,\mu'}\,\delta_{i,i'}, \tag{5}$$

where $\tilde{H}_{{\rm n}\mu}$ indicates one of the Cartesian components of $\tilde{\mathbf{H}}_{\rm n}$. Here $V=(\Delta\tilde{r})^3$ is the discretization volume of the numerical implementation and $\delta_{\mu,\mu'}$ is the Kronecker delta representing the orthogonality of Cartesian coordinates. This result was derived for isolated particles,[9] and interactions between the discretization volumes can be important.[18] To make the simulations tractable, the effect of interactions on the thermal noise has been neglected. Here $\delta(\tilde{t}-\tilde{t}')$ is the Dirac delta function, and its dimensions $[\delta(\tilde{t}-\tilde{t}')]=1/{\rm s}$ are important. After the transformation to dimensionless quantities, the fluctuation-dissipation result is

$$\langle H_{{\rm n}\mu}(\mathbf{r}_i,t)H_{{\rm n}\mu'}(\mathbf{r}_i',t')\rangle=\epsilon\delta(t-t')\,\delta_{\mu,\mu'}\,\delta_{i,i'}, \tag{6}$$

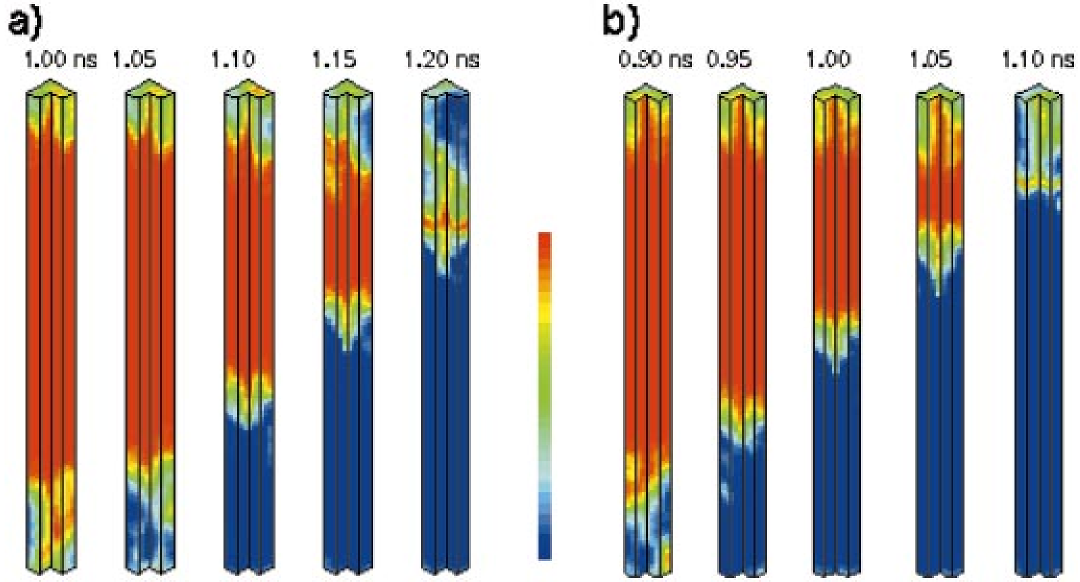

FIG. 1. (Color) Magnetization reversal in the nanoscale magnet after a rapid reversal of the field. The magnets have a square cross section, but are shown in a one-quarter cutaway view. Both reversals are for $H=1800$ Oe and $T=20$ K. Here the z component of the magnetization is shown, with red representing the metastable orientation and blue representing the equilibrium orientation. (a) Nucleation of both end caps, but at different times. (b) Nucleation of one single end cap that grows to reverse the entire magnet.

with the dimensionless strength of the stochastic field given by

$$\epsilon=\frac{2\alpha k_{\mathrm{B}}T}{M_{\mathrm{S}}^{2}V}, \tag{7}$$

where the untransformed discretization volume and saturation magnetization are both used in cgs units to yield the dimensionless result. The dimensionless form of the LLG equation is

$$\frac{d\mathbf{M}(\mathbf{r}_i)}{dt}=\frac{1}{1+\alpha^2}\mathbf{M}(\mathbf{r}_i)\times[\mathbf{H}(\mathbf{r}_i)-\alpha\mathbf{M}(\mathbf{r}_i)\times\mathbf{H}(\mathbf{r}_i)]. \tag{8}$$

This dimensionless stochastic differential equation is used for the numerical integration.

Since the LLG equation conserves the magnitude of the magnetization density, each integration step amounts to a rotation. The size of the tangential displacement at each integration step is given by

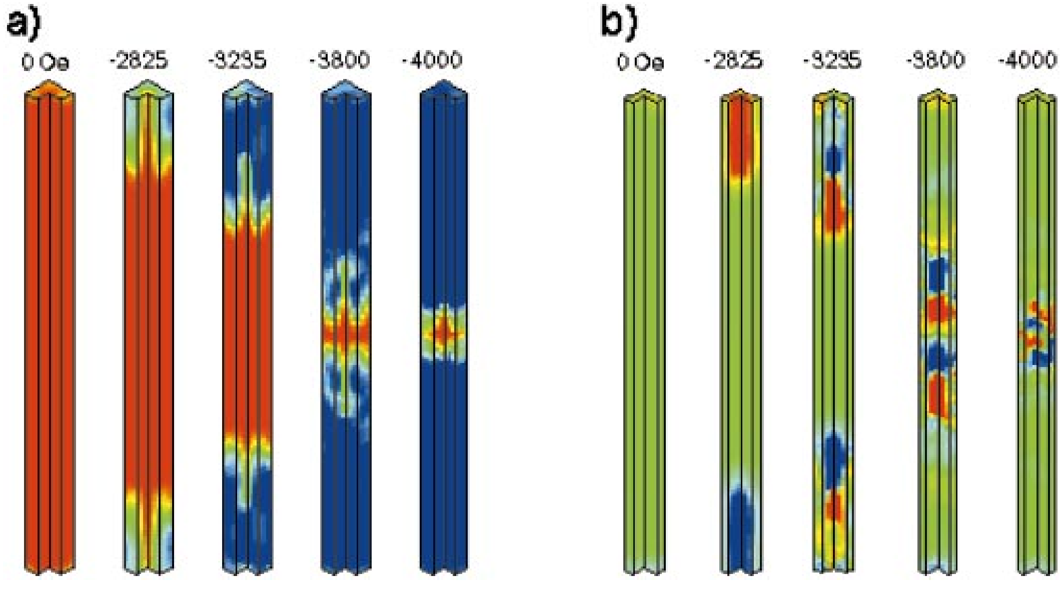

FIG. 2. (Color) Magnetization reversal during a hysteresis loop of 1 ns at $T=0$ K. (a) The z component of the magnetization with the same color scale as in Fig. 1. (b) The magnitude of the curl, $|\mathbf{C}|$, with the sign taken from the value of C_z. Red represents positive curl, blue negative curl, and green zero curl. The fields shown correspond to times 0.25, 0.375, 0.405, 0.45, and 0.5 ns, respectively.

$$\mathbf{R}(\mathbf{r}_i,t)=\frac{1}{1+\alpha^2}\mathbf{M}(\mathbf{r}_i,t)\times[(\mathbf{I}(\mathbf{r}_i,t)-\alpha\mathbf{M}(\mathbf{r}_i,t)\times\mathbf{I}(\mathbf{r}_i,t)], \tag{9}$$

where **I** is the "impulse" over the integration step defined below. The magnetization after the integration step is given by

$$\mathbf{M}(\mathbf{r}_i,t+\Delta t)=\frac{\mathbf{M}(\mathbf{r}_i,t)+\mathbf{R}(\mathbf{r}_i,t)}{\sqrt{1+\mathbf{R}^2(\mathbf{r}_i,t)}}, \tag{10}$$

which ensures the conservation of unit magnitude for **M**. If only the deterministic dynamics were important, a high-order integration method could be used, but to correctly include the thermal noise a lower-order method must be used. Using first-order Euler integration, the impulse including the fluctuating field is

$$\mathbf{I}(\mathbf{r}_i,t)=[\mathbf{H}_{\mathrm{z}}(\mathbf{r}_i,t)+\mathbf{H}_{\mathrm{d}}(\mathbf{r}_i,t)+\mathbf{H}_{\mathrm{e}}(\mathbf{r}_i,t)]\Delta t+\sqrt{\epsilon\Delta t}\,\mathbf{g}(\mathbf{r}_i,t), \tag{11}$$

where $\mathbf{g}(\mathbf{r},t)$ is a random vector with each component chosen independently from a Gaussian distribution of zero mean and unit variance. This result, including the $\sqrt{\Delta t}$ contribution characteristic of integration of stochastic processes, is explained in Appendix B.

III. ISOLATED NANOMAGNETS

The numerical micromagnetic simulation methods described in the previous section have been applied to model nanoscale magnets inspired by those recently fabricated using a combination of chemical vapor deposition and scanning tunneling microscopy techniques by Wirth *et al.*[11,19] The technique has been used to produce arrays of nanoscale magnetic particles with diameters down to about 10 nm and lengths from 50 to 250 nm. The reversal of pillars with diameters more than twice the exchange length, such as these, has been found numerically to proceed by a mode where the magnetization is not constant across the diameter of the pillar.[20–22] The model particles considered here are rectangular prisms 9 nm × 9 nm × 150 nm, which require $N=4949$ sites on the computational lattice. The long axis is taken as the z axis, and the cross-sectional area is chosen comparable to that for a 10-nm-diameter pillar. The external field is always applied along the z axis—the easy axis induced by shape anisotropy. As mentioned in Sec. II, the material parameters were chosen to match those of bulk iron. These are consistent with measurements on the experimentally produced iron nanoparticles.[11,12]

A. Coercive field

Images of the z component of the magnetization, M_z, for such a particle as described above are shown in Fig. 2(a) for several fields during a hysteresis-loop simulation (in a one-quarter cutaway view). The color is a linear scale of M_z, shown in the legend of Fig. 1 with the most negative values at the bottom and the most positive values at the top. For hysteresis-loop simulations, the field is always oriented along the z axis. Starting from its most positive extreme, the value is varied sinusoidally. For the simulation shown in Fig. 2 a period of 1 ns, a field amplitude of 4000 Oe, and a temperature of 0 K were selected. The response of the initially upward-directed magnetization after the applied field is oriented downward can be clearly seen. First, end caps associated with pole avoidance form at both ends. These end caps are regions of high curl in the magnetization density, $\mathbf{C}(\mathbf{r})=\mathbf{\nabla}\times\mathbf{M}(\mathbf{r})$. The end caps are obvious in Fig. 2(b), where $\mathrm{sgn}[C_z(\mathbf{r},t)]|\mathbf{C}(\mathbf{r},t)|$ is shown on a linear color scale, so that right- (left-) handed end caps are colored red (blue). At zero temperature, the two end caps then grow symmetrically until they meet near the midpoint of the particle. While they grow, the area of large curl is concentrated at the interface between the volume where the magnetization has already aligned parallel with the applied field and the volume where it remains antiparallel to the field. Each interface is composed of two regions with opposite z component of the curl, with a curling type of singularity in the center of the pillar. These two regions are separated by a layer where the z component of the curl is close to zero, and the magnetization vectors in the xy plane have a negative divergence located at the center of the pillar. Because the end caps have opposite curls, in the region where the end caps come into contact the curl changes abruptly from large positive to large negative values. Some time is required for this defect to disappear. This reversal of pillars by nucleation of reversed volumes at the ends followed by growth of the reversed regions is consistent with minimization of the micromagnetic energy at zero temperature[23,22] and Monte Carlo simulations at finite temperature,[24] both under quasistatic field-sweep conditions.

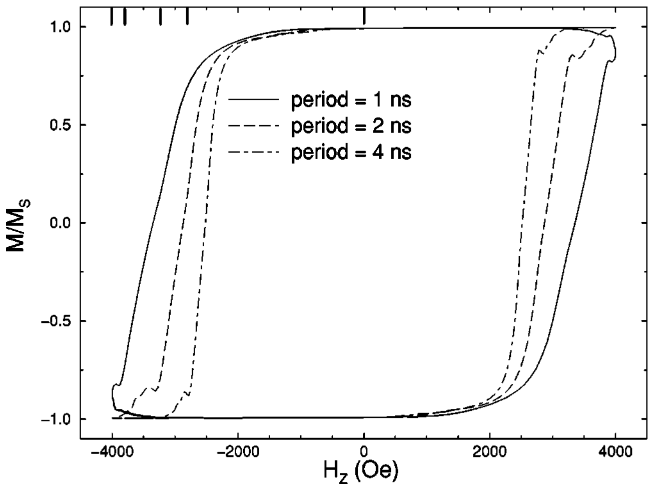

FIG. 3. Hysteresis loops for the individual rectangular pillars at zero temperature and loop periods of 1, 2, and 4 ns. The change in the shape of the loops as the frequency is lowered indicates that the magnetization is not following the applied field in a quasistatic manner. The large tick marks on the upper horizontal axis indicate the times for the images of the magnetization and its curl, shown in Fig. 2

The hysteresis loop associated with this simulation is shown in Fig. 3, with the field values shown in Fig. 2 indicated by large tick marks. Two periods are shown for the 1-ns loop. Aside from differences due to the initial alignment

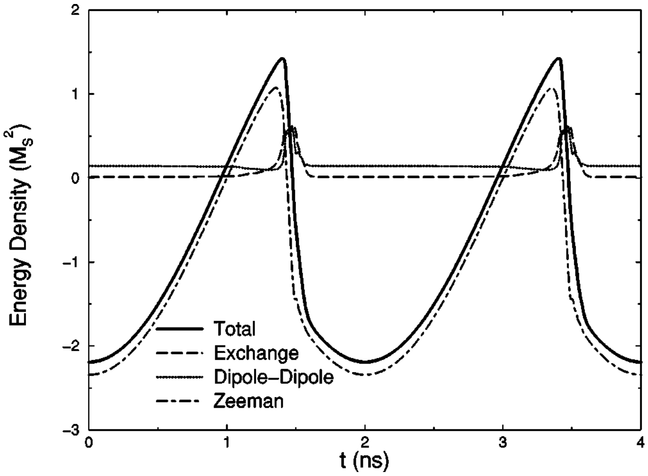

FIG. 4. Energy density vs time for the single hysteresis-loop simulation at $T=0$ K with period 4 ns from Fig. 3. Assuming that the energy is near its metastable minimum before the end caps start to propagate, the coercive field can be estimated from the local maximum in the total energy.

of the magnetization and the presence of the defect after a complete loop, the reproducibility at zero temperature is excellent. Hysteresis loops under the same conditions, but for periods of 2 and 4 ns, are also shown. These simulations show that the hysteresis loop becomes more square for longer periods, indicating that the magnetization is not following the applied field in a quasistatic fashion. This is quite reasonable given that the simulated loops correspond to microwave frequencies, but it makes the infinite-period coercive field difficult to measure.

The average energy density, along with its contributions, as functions of time appears in Fig. 4 for the 4-ns hysteresis loop. The energy density for zero crystalline anisotropy is calculated as

$$E=-\frac{1}{N}\sum_{i=1}^{N}\mathbf{M}(\mathbf{r}_i)\cdot\left(\frac{1}{2}[\mathbf{H}_{\mathrm{e}}(\mathbf{r}_i)+\mathbf{H}_{\mathrm{d}}(\mathbf{r}_i)]+\mathbf{H}_{\mathrm{z}}(\mathbf{r}_i)\right), \tag{12}$$

where N is the number of lattice sites. As the applied field begins to decrease and then become negative, it is the Zeeman energy that changes the most while the exchange and dipole-dipole energies remain nearly constant. Near the coercive field, the exchange energy rapidly increases as regions of reversed magnetization, and the interfaces associated with them, form at the ends of the pillar. Once these reversed regions become large enough, they grow spontaneously and the Zeeman energy rapidly decreases, while the exchange energy from the interface between reversed and unreversed regions remains roughly constant. The growth of the reversed regions does not take long, and the exchange energy quickly dissipates when the regions from the two ends merge at the middle and the reversal is complete.

The information in Fig. 4 can be used for extracting the coercive field of the nanomagnet. For infinitely slow variations in the applied field, dE/dt is proportional to dE/dH_z using the chain rule. Thus portions of the figure with positive slope of the total energy correspond to fields for which the system is trapped behind an energy barrier, while portions with negative slope correspond to fields for which the system responds deterministically by finding a new energy-minimizing magnetization configuration. Fields for which the energy has a maximum should then correspond to the coercive field. Dynamic effects cause the field at which this maximum occurs to depend on the frequency.

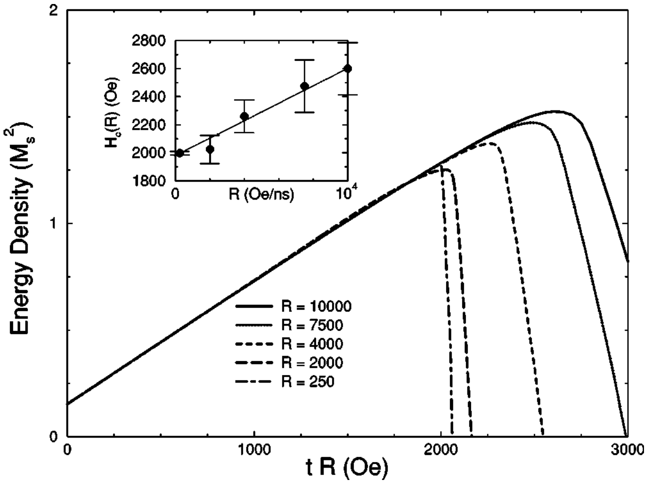

FIG. 5. Total energy density as a function of applied field for fields swept linearly with rate R at zero temperature. The estimation of the zero-rate coercive field H_c estimated from the energy maximum is shown in the inset. The estimated value clearly depends on the rate of change of the applied field, but using linear fitting the static coercive field is found to be 1979 ± 14 Oe. The error bars are estimated using the second derivative at the maximum.

To estimate the static coercive field we find $H_c(R)$ for fields that vary linearly with time, $H(t)=-Rt$ for $t>0$, and then extrapolate to the $H_c(R=0)$ value. The energy density is presented as a function of the absolute value of the applied field in Fig. 5 for rates ranging from $R=250$ Oe/ns to $R=10\,000$ Oe/ns. The coercive fields estimated from the energy maximum are shown in the inset, where the error bars are estimated from the second derivative near the energy maximum. The coercive field clearly decreases with R. Extrapolation of a weighted least-squares fit yields a coercive field of $H_c=1979\pm 14$ Oe at $R=0$. This is a more accurate estimate of the static coercive field than those taken directly from hysteresis-loop simulations.

B. Switching in constant field

At finite temperature the magnetization can reverse, even when the applied field is weaker than the coercive field. In this case, thermal fluctuations carry the magnetization past the free-energy barrier and on to the new equilibrium configuration. Two examples of such thermally induced switching are shown in Fig. 1 for the conditions $H_0=1800$ Oe and $T=20$ K. For small positive times (not shown) the volumes associated with the end caps fluctuate due to the thermal noise. The reversal appears to proceed by a nucleation process, with the end caps serving as the seeds for heterogeneous nucleation. The initiation of the switching from the end caps is similar to results for reversal induced by applied fields greater than H_c in experiments[25] and simulations with $T=0$ K where reversal begins at the end caps[22,26] or corners.[27]

In classical droplet theory, in which boundaries such as the sides of the magnet are ignored, nucleation of the equilibrium magnetization is governed by the competition between the favorable Zeeman energy due to alignment with the applied field and the unfavorable exchange energy due to the interface with the majority volume of the misaligned orientation. The exchange energy dominates for small droplets, which tend to shrink. Large droplets tend to grow because the Zeeman energy dominates. These two regimes are separated by a critical droplet size, the saddle point associated with the free-energy barrier, where the tendencies toward growth and shrinkage are balanced. In nanoscale magnets the situation is more complicated because the free energy cannot be easily separated into surface and volume contributions. Nevertheless, the important aspect remains that a free-energy barrier exists that must be crossed for reversal to begin. The end caps fluctuate until a succession of highly unlikely fluctuations carries the end-cap configuration past the free-energy barrier. After that, growth of the reversed region is energetically favorable and occurs rapidly, on the order of 0.2–0.3 ns for the pillars.

For long pillars, nucleation events at the two ends occur approximately independently of each other. In addition, the growth of a supercritical region takes a significant amount of time: enough time for the other end cap to have a reasonable probability to nucleate and begin to grow. One example of both ends nucleating at different times is shown in Fig. 1(a), while Fig. 1(b) shows nucleation of one end that grows to switch the magnetization of the entire pillar. For the present applied field the latter situation is somewhat rare; from the theory presented below it can be inferred that it occurs in about 10% of simulated switches. From Fig. 1(b) it can also be seen that the nucleation of the two end caps is not completely independent. As one reversed region grows along the pillar, the free-energy barrier at the other end cap decreases. Eventually the free-energy barrier for the second end becomes zero and it will also begin to grow. If a less negative field is applied, the free-energy wells of the metastable states will be deeper and the first reversed region will have to grow further along the pillar before this occurs.

The mean switching time $\overline{t}_{\mathrm{sw}}$, defined here as the first time when $M_z=0$, is shown in Fig. 6(a) as a function of applied field for $T=20$ K. The difference in the error bars reflects the amount of statistical sampling at the different conditions. The dependence of $\overline{t}_{\mathrm{sw}}$ on temperature is shown in Fig. 6(b) for applied fields of $H_0=1850$ Oe; fields are always applied along the pillar. While there is a clear dependence on field and temperature, we find no clear functional form for the dependence. Notably, the exponential dependence of $\overline{t}_{\mathrm{sw}}$ on inverse temperature, expected when the barrier is high, is not seen. This implies that the free-energy barrier is low. In fact, this picture is consistent with the switching statistics described next, where the dynamics are consistent with a biased walk in a shallow well.

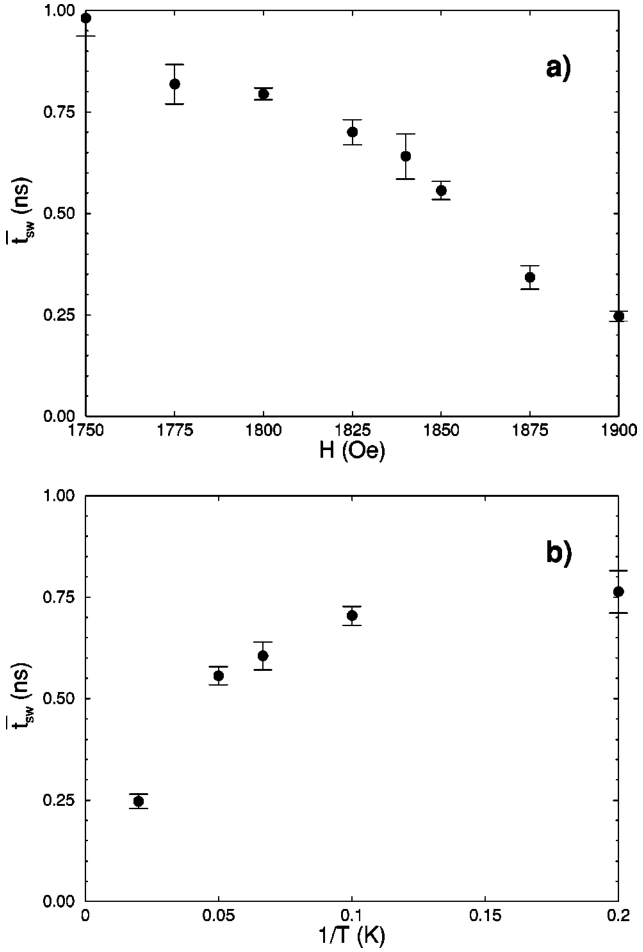

FIG. 6. Mean switching time as a function of (a) applied field at $T=20$ K and (b) temperature at $H=1850$ Oe. The switching time increases as (a) the free-energy barrier separating the metastable and stable orientations grows as the applied field is decreased or (b) the thermal energy available for crossing the barrier decreases as temperature is lowered.

The statistics of magnetization switching are measured by $P_{\mathrm{not}}(t)$, the probability of not switching before time t. The simulation results for $P_{\mathrm{not}}(t)$ for 200 switches at $H_0=1800$ Oe and $T=20$ K are presented in Fig. 7(a). The result is clearly not exponential, the expected functional form when the free-energy barrier is large. Experimental results for single-domain magnets, in which $P_{\mathrm{not}}(t)$ is not exponential, have been reported recently.[28]

A simple theory that assumes completely independent nucleation at the two ends of the pillar produces a reasonable description of the simulation result. The theory for $P_{\mathrm{not}}(t)$ requires two parameters. The first is the constant nucleation rate $\mathcal{I}$ for the formation of a supercritical reversed region at one isolated end of a pillar. The second is the rate v at which a single growing region changes the normalized magnetization of the pillar. Labeling the two independent nucleation times at the top and bottom t_{t} and t_{b}, respectively, the positive values of the magnetization of the pillar can be described by

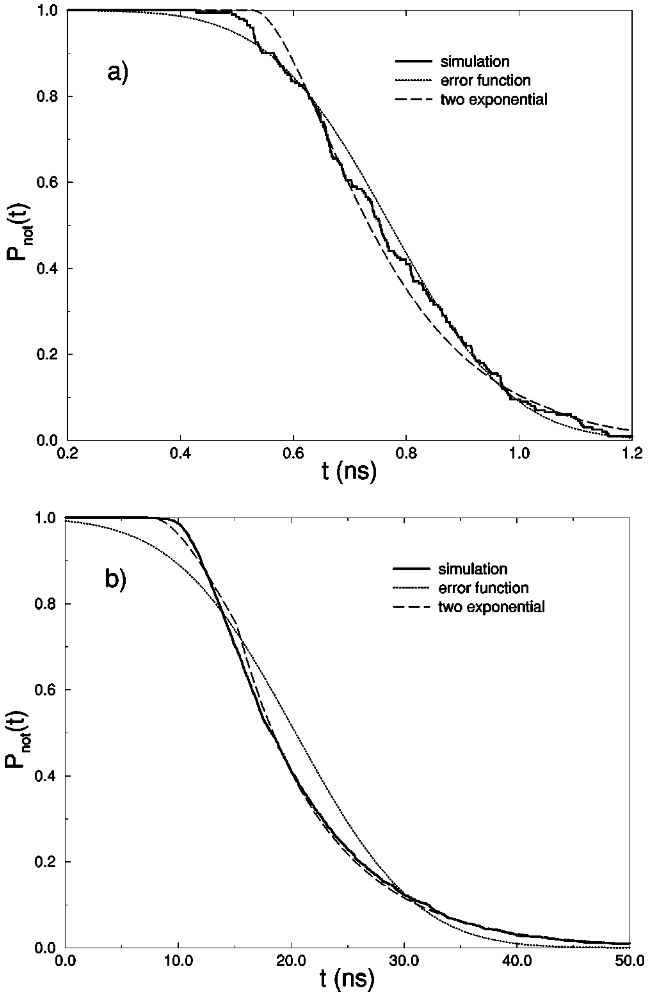

FIG. 7. Probability of not switching, $P_{\rm not}(t)$, for (a) 200 switches of nanoscale magnetic pillars at $H=1800$ Oe and $T=20$ K, and (b) 2000 switches in a simple one-dimensional model nanopillar at $H=1000$ Oe and $T=20$ K. The theoretical forms, Eqs. (15) and (16), were fitted by matching their first and second moments to those of the simulation data.

$$M_z(t)=\begin{cases}1, & t<t_1,\\ 1-v(t-t_1), & t_1\leqslant t<t_2,\\ 1-v(t-t_1)-v(t-t_2), & t_2\leqslant t,\end{cases} \tag{13}$$

where $t_1=\min(t_{\rm t},t_{\rm b})$ and $t_2=\max(t_{\rm t},t_{\rm b})$. We define switching to occur at $M_z(t_{\rm sw})=0$, when roughly one-half the volume of the nanomagnet is oriented in the equilibrium direction. The switching can occur either through one or both ends nucleating, and the actual switching time for a particular $(t_{\rm t},t_{\rm b})$ is given by

$$t_{\rm sw}=\min\left(2t_0+t_1, t_0+\frac{t_1+t_2}{2}\right), \tag{14}$$

where $t_0=1/(2v)$ is the earliest time at which the pillar can switch. For times $t<t_0$ the probability of switching is zero, even if both ends nucleate immediately after the reversal. The situation in the $t_{\rm b}$-$t_{\rm t}$ plane is shown in Fig. 8, where the dashed curves correspond to two different conditions of constant $t_{\rm sw}$, $t_{\rm sw}/t_0=3/2$ and 3. The solid lines divide the plane into regions with different switching histories. In the triangle near the origin (I), switching occurs for times $t_0<t_{\rm sw}<2t_0$, which can happen only if both ends nucleate. Between the parallel solid lines (II) switching occurs by double nucleation, while outside them (III and IV) a single nucleation causes the switching. Since each nucleation process has a constant rate, the corresponding probability density function for the nucleation time is exponential, $\mathcal{I}\exp(-\mathcal{I}t)$. Integrating along curves of constant $t_{\rm sw}$, the probability of not switching before time t is found to be[3]

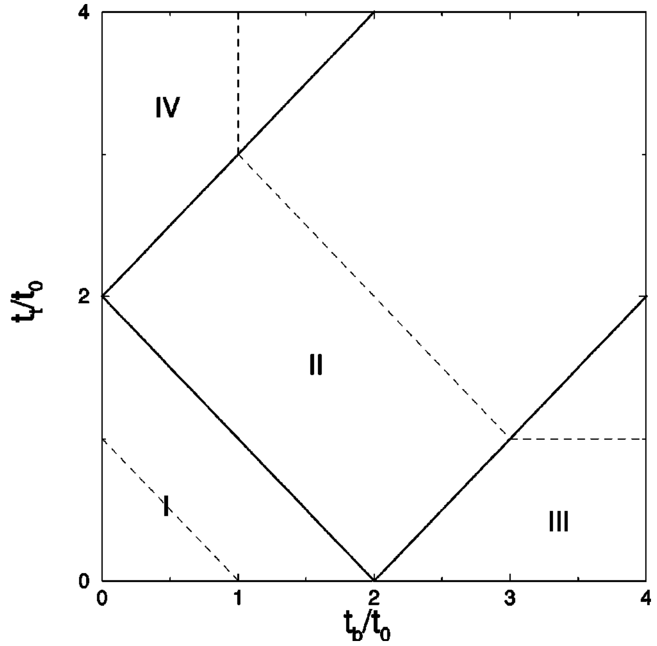

FIG. 8. Integration of weights to get $P_{\rm not}(t)$, Eq. (15). The solid lines separate regions where one (or two) nucleation events occur before switching, while the dashed curves are integration paths for constant switching time, $t_{\rm sw}/t_0=3/2$ and 3. See the text for a full explanation.

$$P_{\rm not}(t)=\begin{cases}1, & t<t_0,\\ e^{-2\mathcal{I}(t-t_0)}[1+2\mathcal{I}(t-t_0)], & t_0\leqslant t<2t_0,\\ e^{-2\mathcal{I}(t-t_0)}[1+2\mathcal{I}t_0], & 2t_0\leqslant t.\end{cases} \tag{15}$$

We will refer to this as the "two-exponential" decay model. In the limit of infinitely fast growth, $t_0=0$, only regions III and IV remain, and this becomes a simple exponential decay associated with thermally activated crossing of a free-energy barrier. For $t_0>0$, $P_{\rm not}(t)$ is quadratic in $t-t_0$ for $t\rightarrow t_0^+$, has a discontinuity in the slope at $t=2t_0$, and is exponential for $t>2t_0$.

The fit of the two-exponential decay model of Eq. (15) to the simulation results appears in Fig. 7(a) as the dashed curve. The dotted curve is a fit to the error function

$$P_{\rm erf}(t)=\frac{1}{2}-\frac{1}{2}{\rm Erf}[\tilde{\mathcal{I}}(t-\tilde{t}_0)], \tag{16}$$

which was chosen as an empirical form because it also has two adjustable parameters, chosen here to have a similar interpretation as the theory given above. The parameters for both theoretical forms were determined by matching the first and second moments of the theoretical form to the moments of the simulation data, and the parameters are $\mathcal{I}\approx 4.049$, $t_0 \approx 0.527$ and $\tilde{\mathcal{I}}\approx 4.176$, $\tilde{t}_0 \approx 0.790$. For these conditions, both forms, Eqs. (15) and (16), seem to fit the simulation data about equally well. The disagreement with Eq. (15) probably occurs because the condition that the free-energy barrier be much greater than $k_{\rm B}T$ is not met. When the free-energy barrier is much less than $k_{\rm B}T$, the magnetization should be more like a biased random walk. In that case the most noticeable effect of thermal fluctuations would be a symmetric smearing of the switching times around $\overline{t_{\rm sw}}$.

The question of statistical sampling is also important. Specifically, one expects to have undersampling of the population because the finite-sampling $P_{\rm not}(t)$ goes to zero faster than the infinite-sampling $P_{\rm not}(t)$ with increasing t. In fact, for times less than the maximum observed switching time in the long-time tail of the distribution, the error function underestimates the population, while the two-exponential theory overestimates it. To this extent, it is possible that data with better sampling may shift towards better agreement with Eq. (15). Indeed, experimental switching probabilities[28] in single-domain magnets have been observed to have exponential tails, which is inconsistent with Eq. (16).

Better statistics and a higher free-energy barrier are needed to validate the theoretical $P_{\rm not}(t)$ given in Eq. (15). For the present model, better statistics would be prohibitive; the 200 switches considered here took approximately 20 weeks to generate using 4 processors on an Origin 2000. A less realistic but numerically faster simulation, in which the pillars are modeled as one-dimensional stacks of cubes, is presented in the next section. The advantage of this simplified model is that it allows many more switching events to be observed in a reasonable amount of computer time, even with much higher free-energy barriers. This improves the statistics for the very rare events with $t_{\rm sw} \gg 2t_0$ and $t_{\rm sw} \rightarrow t_0$, which are important to distinguish between alternative theoretical forms for $P_{\rm not}(t)$.

IV. SIMPLE MODEL

In order to generate a sufficiently large sample of switching events in nanoscale magnets, we consider a simpler model in which the pillar consists of a one-dimensional stack of cubic cells, which is the model introduced by Boerner and Bertram.[29] The cubes have a linear size $\Delta\tilde{r} = 2l_{\rm e}$, here 5.2 nm, since the material parameters for iron are used (Ref. 29 used parameters for nickel). To keep the aspect ratio of the nanopillars as close as possible to those considered above, a pillar composed of 17 cubes is used. For this simple model, the local field due to the dipole interactions is calculated as[29]

$$\tilde{\mathbf{H}}'_{\rm d}(\tilde{\mathbf{r}}_i) = (\Delta\tilde{r})^3 \sum_{j\neq i} \frac{3\hat{\mathbf{r}}_{ij}[\hat{\mathbf{r}}_{ij}\cdot\tilde{\mathbf{M}}(\tilde{\mathbf{r}}_j)] - \tilde{\mathbf{M}}(\tilde{\mathbf{r}}_j)}{\tilde{\mathbf{r}}_{ij}^3}, \qquad (17)$$

where $\tilde{\mathbf{r}}_{ij}$ is the displacement vector from the center of cube i to the center of cube j, and $\hat{\mathbf{r}}_{ij}$ is the corresponding unit vector. The factor of volume $(\Delta\tilde{r})^3$ results from integrating over the constant magnetization density in each cell. This factor can be combined with $\tilde{r}_{ij}^3$, so that the denominator depends only on $\mathbf{x}_{ij} = \tilde{\mathbf{r}}_{ij}/(\Delta\tilde{r})$, which is a vector of integers denoting the difference in cell indices. It can readily be seen that for a uniformly magnetized pillar the summation over index integers leads to different values of $\mathbf{H}'_{\rm d}(\mathbf{r})$ for different choices of discretization length along the long axis. This happens because self-contributions have been ignored and the far-field result has been used for neighboring cells. However, since this model is being used to investigate only the statistics of switching, and not for estimating physical values, the results should be qualitatively correct. Using the scaling to dimensionless units, the approximate dipole field is

$$\mathbf{H}'_{\rm d}(\mathbf{r}_i) = \sum_{j\neq i} \frac{3\hat{\mathbf{r}}_{ij}[\hat{\mathbf{r}}_{ij}\cdot\mathbf{M}(\mathbf{r}_j)] - \mathbf{M}(\mathbf{r}_j)}{\mathbf{x}_{ij}^3}. \qquad (18)$$

We have verified that our implementation of the model agrees with that of Boerner and Bertram by reproducing the observed coercive field for the nickel pillars discussed in Ref. 29. Because of the different approximations, the coercive field for the present iron pillars is about 1500 Oe.

The probability of not switching for 2000 switches for this model of iron pillars is shown in Fig. 7(b), along with the two theoretical forms, Eqs. (15) and (16), which have been fit using the same procedure as in Sec. III. The kink in the two-exponential theoretical form at $2t_0$ is quite noticeable, but cannot be seen in the simulation data. The kink has its origin in the complete suppression of nucleation for negatives times, and the absence of the kink in the simulation data may stem from the finite chance of nucleation at negative times due to the way the field is reoriented, as described in Sec. III A. Another possibility is that the interactions between the ends smooth out the difference between the one- and two-nucleation decay modes. Despite the kink, the theoretical form, Eq. (15), does a good job of describing both the exponential tail and the rounding at early times of $P_{\rm not}(t)$. It is clearly superior to the error-function form, as well as to a displaced, single exponential (not shown).

V. ARRAYS OF NANOMAGNETS

The long-ranged dipole-dipole interactions that contribute to the shape anisotropy of nanoscale magnets also cause interactions between nanomagnets. This is especially true in most potential applications, where miniaturization will drive devices to high densities. In addition, the interactions between nanomagnets in arrays could be the basis of device applications, prototypes of which have already been investigated.[30,31] Regular arrays of nanomagnets have already been used experimentally to provide magnetic signals strong enough to be measured[11,19] in the experiments our nanomagnets are modeled after. Our simulations show that even for very wide spacings the magnetic interactions be-

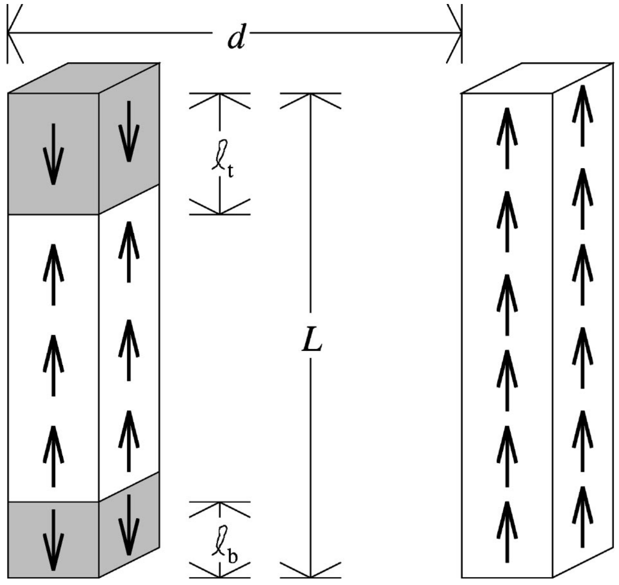

FIG. 9. Schematic of two pillars, one with a growing region of magnetization in the equilibrium orientation at each end. The distance between pillars is d, their height is L, and the length of the reversed regions along the long axis are l_t and l_b, respectively.

tween nanomagnets have significant effects on the switching properties.

To allow for analytic treatment, we consider only the two leading contributions to the local dipole field $\mathbf{H}_{\mathrm{d}}(\mathbf{r})$ from the dipole and quadrupole moments of the source magnet. The former contributes uniformly throughout the observation volume, while the latter changes linearly in each Cartesian direction. Specifying the distance between pillars as d and considering the dipolar and quadrupolar moments of the source magnet, M_1^0 and M_2^0, respectively, the leading contributions to the observed demagnetizing field are $\mathbf{H}_{\mathrm{d}}^{(1)}(\mathbf{r}) = -\hat{\mathbf{e}}_{\mathrm{z}} M_1^0/d^3$ and $\mathbf{H}_{\mathrm{d}}^{(2)}(\mathbf{r}) = -9(2z\hat{\mathbf{e}}_{\mathrm{z}} - x\hat{\mathbf{e}}_{\mathrm{x}} - y\hat{\mathbf{e}}_{\mathrm{y}})M_2^0/(4d^5)$, respectively. Simple expressions for the multipole moments can be calculated in the following way. Assume a pillar with regions of uniform magnetization oriented in the $+\hat{\mathbf{e}}$ direction in the middle and in the $-\hat{\mathbf{e}}$ direction at the ends, as shown in Fig. 9. With the total pillar length L, the top-region length l_{t}, and the bottom-region length l_{b} all measured along the long axis of the pillar, the dipole moment for a reversing pillar is

$$M_1^0 = M_{\mathrm{S}} A(L - 2l_{\mathrm{t}} - 2l_{\mathrm{b}}) \tag{19}$$

and the quadrupole moment is

$$M_2^0 = 2M_{\mathrm{S}} A[l_{\mathrm{t}}^2 - l_{\mathrm{b}}^2 - L(l_{\mathrm{t}} - l_{\mathrm{b}})], \tag{20}$$

where A is the cross-sectional area of the pillar. The dimensionless form is achieved by setting M_{S} to unity and using dimensionless lengths.

Using the simplified expression for the dipole moment in Eq. (19), the contribution from one upward-magnetized pillar at the nearest-neighbor position in the array is $\mathbf{H}_{\mathrm{d}}^{(1)} \cdot \hat{\mathbf{e}}_{\mathrm{z}} \approx -1$ Oe. The quadrupole contribution from Eq. (20) at the end of one nanomagnet that is the nearest neighbor to a switching pillar with $l_{\mathrm{t}} = L/2$ is $\mathbf{H}_{\mathrm{d}}^{(2)} \cdot \hat{\mathbf{e}}_{\mathrm{z}} \approx 0.4$ Oe. This is a rough estimate of the maximum interaction through the quadrupole moment, and the sign indicates a tendency for neighboring pillars in the array to switch at opposite ends.

As a simple initial investigation, we consider a linear array of four of the rectangular nanomagnets described in Sec. III, with the nanomagnets oriented perpendicular to the substrate. Since dipole-dipole interactions within each nanomagnet are calculated using the fast multipole method described in Appendix A, the multipole moments for each nanomagnet are readily available. These moments can be used to quickly calculate the interactions between nanomagnets in the array, under the constraint that the far-field description is appropriate. To ensure this we have considered only a spacing between pillars of two pillar lengths, 300 nm. Note that this situation is quite different from fast fourier transform approaches, in which the calculation must be carried out on a lattice that also fills the space *between* the nanomagnets.[32] To do that practically, the space between the magnets must be kept small.

To study arrays of nanomagnets, systems consisting of four 9 nm$\times$9 nm$\times$150 nm parallel pillars arranged in a line perpendicular to their long axes and spaced 300 nm apart were simulated using the fast multipole method truncated at $p=3$. Hysteresis loops with periods on the order of a few nanoseconds for the individual pillars in the array look similar to those for isolated pillars in Fig. 3, with no observable difference between pillars on the outside and those on the inside of the array. The symmetry equivalence for the two pillars on the inside, and for the two pillars on the outside, will be used throughout to double the statistical sampling.

The probability of not switching for $H=1800$ Oe and $T=20$ K is shown for 40 array switches in Fig. 10(a) for pillars on the inside and outside of the array, as well as isolated pillars. No significant difference can be seen between the three curves. However, the coupling between the pillars can be seen in the difference between the $P_{\mathrm{not}}(t)$ for inside pillars with one or both nearest-neighbor pillars switched, shown in Fig. 10(b). Here, t is the time difference between t_{sw} and the last time a neighboring pillar switched. From these data it can be seen that of pillars with two neighbors, those with only one neighbor switched tend to switch earlier than those with both pillars switched. The effect is even more pronounced in simulations of the simple model at $H=1000$ Oe.[5]

VI. SUMMARY

Numerical simulation of the Landau-Lifshitz-Gilbert micromagnetic model has been used to investigate spatially nonuniform magnetization switching in nanoscale magnets at the nanosecond time scale. We have focused on iron pillars 9 nm$\times$9 nm$\times$150 nm because such pillars and arrays have been constructed and measured experimentally.[11,19] The zero-temperature static coercive field has been estimated numerically to be $H_c = 1979 \pm 14$ Oe by finding the field of maximum energy for fields swept at constant rate and then extrapolating to find the zero-rate estimate. Simulations of

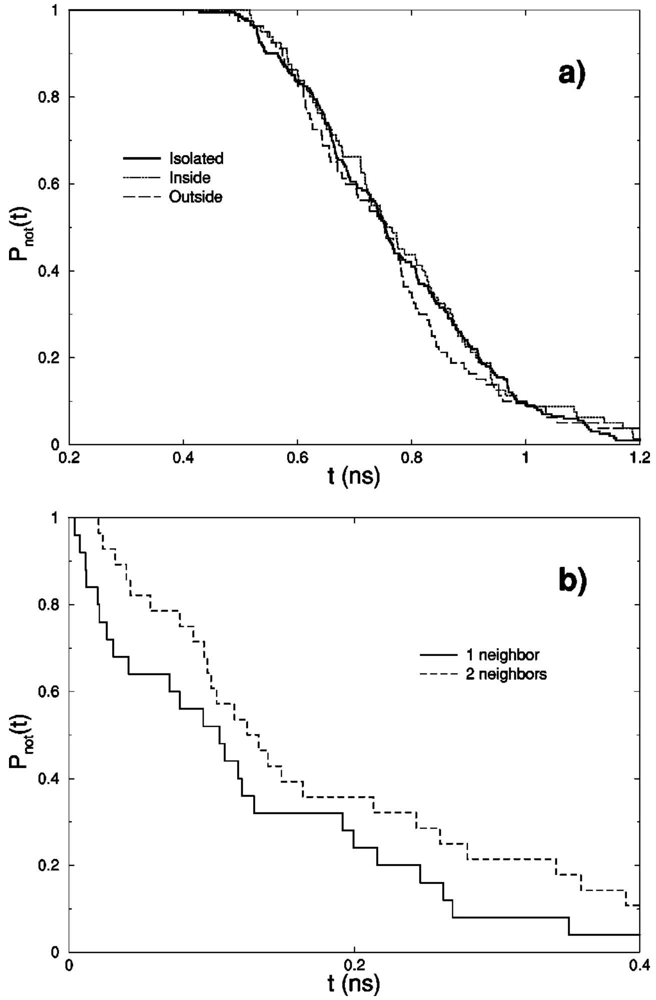

FIG. 10. (a) Probability of not switching, $P_{\mathrm{not}}(t)$, for nanoscale magnetic pillars in a four-pillar array at $H=1800$ Oe and $T=20$ K. The two pillars on the outside and the two on the inside are equivalent by symmetry. The isolated pillar data are the same as in Fig. 7. (b) Interactions between pillars as seen in the difference between $P_{\mathrm{not}}(t)$ for inside pillars with one and both neighboring pillars already switched. Here $t=0$ corresponds to the time of the most recent switch of a neighboring pillar.

thermally activated magnetization switching are possible at fields well below the coercive value. For the pillars studied here, reversal occurs through nucleation at the ends of the pillars. The probability of not switching, $P_{\mathrm{not}}(t)$, is not well described by a delayed exponential, and a theoretical form, Eq. (15), based on independent nucleation at the ends of the magnet is developed here. The agreement with results for intensive, fully three-dimensional simulations with an applied field near the coercive value is reasonable, but an *ad hoc* error function gives similar agreement. The agreement with Eq. (15) is much better when the field is well below the coercive value and the statistics are better, which currently we have only studied with less-intensive simulations that discretize the nanomagnet only along its long axis.

The fully three-dimensional micromagnetics program has been developed for massively parallel computers and implemented using the fast multipole method. These two features make it feasible to simulate nanomagnets in widely spaced arrays. Even though the interactions between the magnets are quite weak for the specific linear array considered here, there are significant effects on the statistics of the magnetization switching. Specifically, there is a dependence of $P_{\mathrm{not}}(t)$ for a given pillar on the orientation of the magnetization of its nearest neighbors in the array. The nature of the cooperative reversal mode observed here is a topic for future research.

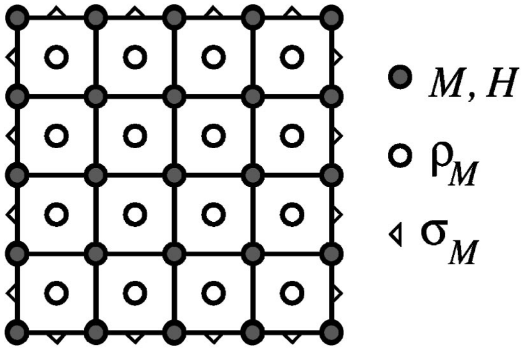

FIG. 11. Schematic of the relationship between the lattice and the dual lattices, projected along the z axis. The magnetization density $\mathbf{M}(\mathbf{r}_i)$ and the local magnetic field $\mathbf{H}(\mathbf{r}_i)$ are known at the lattice sites of the simple cubic lattice (solid circles), the magnetic charge density ρ_{M} is known at the dual lattice sites (open circles) which are located at the body center positions, and the magnetic surface charge density is known at the centers of squares defined by the surface lattice sites (open triangles).

ACKNOWLEDGMENTS

This work was supported by NSF Grant No. DMR-9871455, Florida State University (FSU) Center for Materials Research and Technology, the FSU Supercomputer Computations Research Institute (U.S. DOE Contract No. DE-FC05-85ER25000), and the FSU School of Computational Science and Information Technology. Extensive supercomputer resources were provided by FSU Academic Computing and Network Services and by the U.S. Department of Energy through the U.S. National Energy Research Scientific Computing Center.

APPENDIX A

Calculating the dipole-dipole interactions is the most intensive part of the numerical calculation. The magnetic potential approach used here involves defining a magnetic charge density $\rho_{\mathrm{M}}(\mathbf{r})=-\boldsymbol{\nabla}\cdot\mathbf{M}(\mathbf{r})$. (We present this only in terms of the dimensionless quantities.) This charge was evaluated on a cubic lattice dual to that of $\mathbf{M}(\mathbf{r}_i)$ (see Fig. 11) using equally weighted two-point differences, specifically,

$$\rho_{\mathrm{M}}(\mathbf{r}_{\mathrm{d}})=-\sum_{\mu=1}^{3}\left(\frac{1}{4\Delta r}\sum_{|\mathbf{h}|=\sqrt{3}\Delta r/2}\mathrm{sgn}(\mathbf{h}\cdot\hat{\mathbf{e}}_{\mu})\mathbf{M}(\mathbf{r}_d+\mathbf{h})\cdot\hat{\mathbf{e}}_{\mu}\right), \tag{A1}$$

where $\mathbf{r}_\mathrm{d}$ is a position on the dual lattice, $\Sigma_\mathbf{h}$ is the sum over the corresponding corners of the cube from the direct lattice, and $\hat{\mathbf{e}}_\mu$ are the Cartesian unit vectors. If we were to apply Eq. (A1) with $\mathbf{r}_\mathrm{d}$ just outside the magnetic material, it would give a nonzero charge there. To avoid this unphysical result, we have moved this charge to the surface by defining a surface magnetic charge density $\sigma_\mathrm{M}(\mathbf{r}) = \hat{\mathbf{s}}(\mathbf{r}) \cdot \mathbf{M}(\mathbf{r})$, where $\hat{\mathbf{s}}$ is the unit vector directed out of the surface. We have considered surface charges only on the surface of the model magnet, and we evaluate them at the centers of the squares defined by adjacent points on the surface of the direct lattice. The four corners are equally weighted so that

$$\sigma_\mathrm{M}(\mathbf{r}_{\mathrm{d}'}) = \frac{1}{4} \sum_{|\mathbf{h}| = \sqrt{2}\Delta r/2} \hat{\mathbf{s}} \cdot \mathbf{M}(\mathbf{r}_{\mathrm{d}'} + \mathbf{h}), \tag{A2}$$

where $\Sigma_\mathbf{h}$ runs over the four corners. The numerical approach of Eqs. (A1) and (A2) ensures that there is no net magnetic charge on the system as a whole.

The magnetic potential $\phi_\mathrm{M}(\mathbf{r})$ is found by integrating over both the volume and surface charges,[33]

$$\phi_\mathrm{M}(\mathbf{r}) = \int_\mathrm{V} d\mathbf{r}' \frac{\rho_\mathrm{M}(\mathbf{r}')}{|\mathbf{r} - \mathbf{r}'|} + \oint_\mathrm{S} d\hat{\mathbf{s}}' \frac{\sigma_\mathrm{M}(\mathbf{r}')}{|\mathbf{r} - \mathbf{r}'|}. \tag{A3}$$

Numerically, such an operation can be quite expensive since unsophisticated algorithms will require $O(N^2)$ operations, where N is the number of lattice sites. An algorithm that remains reasonable for large systems is the fast multipole method.[17]

We have chosen to calculate the magnetic potential using the fast multipole method (FMM) because it has several advantages over the more traditional fast Fourier transform (FFT) approach. The biggest difference between the two methods is that the FMM makes no assumptions about the underlying lattice, while the FFT method assumes a cubic lattice with periodic boundary conditions. One consequence of this assumption is that numerical models of systems without periodic boundary conditions require empty space around the magnet so that the boundary conditions do not affect the calculation. The FFT method also requires the lattice to continue into regions of empty space that lie between elements of an array of magnets. By contrast, a FMM implementation only needs to consider volumes occupied by magnetic material. It does not need any padding. In addition to these advantages, the FMM is more efficient for large numbers of lattice sites.

The popularity of the FFT approach stems from the fact that it takes $O(N \ln N)$ calculations to evaluate Eq. (A3). The FMM has a larger overhead, but requires only $O(N)$ operations to calculate the same potential.[17] This means that a FFT approach to Eq. (A3) makes sense for small, cubic lattices, but that the FFM approach will be more efficient for large, irregular, or incomplete lattices.

The FMM algorithm exploits the fact that ϕ_M at each lattice point can be expanded in terms of spherical harmonics,

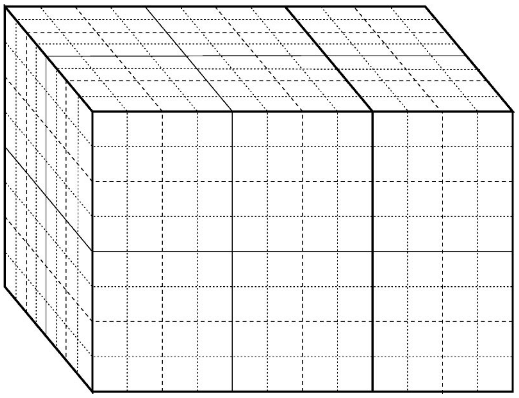

FIG. 12. Schematic of the hierarchical decomposition of space chosen for our implementation of the fast multipole method. This eightfold decomposition at each level is quite efficient given the underlying cubic lattice.

$$\phi_\mathrm{M}(r, \theta, \varphi) = \sum_{i=0}^{\infty} \sum_{j=-i}^{i} \left(L_i^j r^i + \frac{M_i^j}{r^{i+1}} \right) Y_i^j(\theta, \varphi), \tag{A4}$$

where the L_i^j terms can be used to represent the potential close to the lattice point, and the M_i^j terms can be used to represent the potential far from it, but not both simultaneously. In this context, near $\mathbf{r}_i$ means being closer to $\mathbf{r}_i$ than any other lattice point, and far means distances more than twice the largest distance from the center of cell j to any of its boundary points. Following Greengard,[17] we define the spherical harmonics

$$Y_i^j(\theta, \varphi) = \sqrt{\frac{(i - |j|)!}{(i + |j|)!}} P_i^{|j|}(\cos\theta) e^{Ij\varphi}, \tag{A5}$$

with $P_i^j(x)$ the associated Legendre polynomial, and $I = \sqrt{-1}$. Actually implementing this approach requires a truncation of the expansion in i at order p. We have found that the demagnetizing field for $p = 3$ is within 1% of the exact value for our simulations.

Our implementation of the FMM algorithm starts by partitioning the model space into a system of cubes; an example is shown in Fig. 12. The length of the side of the smallest cubes, which are separated by dotted lines, is the same as the discretization length. For our lattice system we have found that the most efficient choice is to use cubes centered on the *direct* lattice. For each cube, the multipole expansion coefficients of the far-field potential are calculated for the specific configuration of magnetic charges ρ_M and σ_M,

$$M_i^j = \int_V d\mathbf{r} [\rho_\mathrm{M} + \sigma_\mathrm{M}] \varrho^i Y_i^j(\theta, \varphi), \tag{A6}$$

with the coordinates centered on the lattice site. Note here that ϱ^i is the distance from the center of the cell raised to the ith power. For our cubic lattice, each quadrant of the cube is contributed by a different region of constant ρ_M from the dual lattice (similarly for σ_M). With the geometry of the lattice fixed, the multipole expansion coefficients are easily calculated and summed to yield the total expansion coefficients for the lattice site.

Each level of the hierarchy involves grouping cells into successively larger cubes that completely contain cubes at the lower level. The obvious hierarchy with each larger cube containing eight of the smaller cubes apparently works best. In Fig. 12, cubes of the second level are separated by dashed lines and those of the third level by solid lines. Since the number of nodes in any direction along the simulation lattice is not restricted to a power of two, cubes do not always contain eight smaller cubes. The M_i^j for the larger cube can be rapidly evaluated from those of the smaller cubes using the rule for translation of a multipole expansion,[17]

$$M_i^j = \sum_{k=0}^{i} \sum_{l=-k}^{k} O_{i-k}^{j-l} \frac{J_l^{j-l} A_k^l A_{i-k}^{j-l}}{A_i^j} \varrho^k Y_k^{-l}(\theta,\varphi), \tag{A7}$$

where O_i^j are the expansion coefficients for the smaller cube and the spherical coordinates (ϱ,θ,φ) here are for the vector from the origin of the large cube to that of the small cube. The relations for the new factors are[17]

$$A_i^j = \frac{(-1)^j}{\sqrt{(i-j)!(i+j)!}} \tag{A8}$$

and

$$J_i^j = \begin{cases} (-1)^{\min(|i|,|j|)} & \text{if } ij<0, \\ 1 & \text{otherwise.} \end{cases} \tag{A9}$$

The construction of the hierarchy terminates when the entire system is enclosed by a single cube. The partitioning can be generalized to noncubic rectangular prisms, but the restriction that the multipole expansion is only valid at distances larger than twice the diagonal of the rectangle will complicate the algorithm.

A downward pass through the hierarchy involving three types of operations is required to construct ϕ_{M} as represented by the local expansion coefficients L_i^j for each cube. The first operation is the translation of the local expansion for the encompassing bigger cube (if one exists) that includes all the contributions from its far field, i.e., those cubes on its level that are not its neighbors. This translation is accomplished by the rule[17]

$$L_i^j = \sum_{k=i}^{p} \sum_{l=-k}^{k} O_{k,l} \frac{\overline{J}_{k-i,l-j}^{l} A_{k-i}^{l-j} A_i^j}{A_k^l} \varrho^{k-i} Y_{k-1}^{l-j}(\theta,\varphi), \tag{A10}$$

where O_i^j are the local expansion coefficients of the larger cube, and the spherical coordinates (ϱ,θ,φ) here are for the vector from the origin of the smaller cube to that of the larger cube. A_i^j is defined in Eq. (A8), while[17]

$$\overline{J}_{i,j}^{k} = \begin{cases} (-1)^i(-1)^j & \text{if } jk<0, \\ (-1)^i(-1)^{k-j} & \text{if } jk>0 \text{ and } |k|<|j|, \\ (-1)^i & \text{otherwise.} \end{cases} \tag{A11}$$

The next operation incorporates the contributions from areas in the near region of the larger cube, but in the far region of the smaller cube. This is accomplished by transforming the multipole expansion of the source into a local expansion of the smaller cube using[17]

$$L_i^j = \sum_{k=0}^{p} \sum_{l=-k}^{k} O_k^l \frac{\tilde{J}_k^{j,l} A_k^l A_i^j}{A_{i+k}^{l-j}} \frac{Y_{i+k}^{l-j}(\theta,\varphi)}{\varrho^{i+k+1}}, \tag{A12}$$

where the spherical coordinates are for the vector from the origin of the smaller cube to that of the larger cube and[17]

$$\tilde{J}_i^{j,k} = \begin{cases} (-1)^i(-1)^{\min(|j|,|k|)} & \text{if } jk>0, \\ (-1)^i & \text{otherwise.} \end{cases} \tag{A13}$$

The third type of operation is used for termination of the algorithm at the lowest level, where the near-region contributions for the smallest cubes must be evaluated exactly. Since a regular lattice is used, the point $\mathbf{r}_i$ where ϕ_{M} is being calculated always lies at the corner of the neighboring cube of constant ρ_{M}, and the contribution is simply

$$\frac{(\Delta r)^2}{8}\left[6\sinh^{-1}\left(\frac{1}{\sqrt{2}}\right) - \frac{\pi}{2}\right]\rho_{\mathrm{M}}(\mathbf{r}_d), \tag{A14}$$

because only one quadrant of the region of constant ρ_{M} needs to be considered in this exact manner. The contribution for squares of surface charge that touch $\mathbf{r}_i$ is

$$\Delta r \sinh^{-1}(1)\sigma_{\mathrm{M}}(\mathbf{r}_d). \tag{A15}$$

Similar expressions can be calculated for general rectangular prisms.

The FMM is an efficient way of determining the magnetic potential $\phi_{\mathrm{M}}(\mathbf{r}_i)$ associated with a particular configuration of a dipole field. The local observed magnetic field due to the other dipoles is obtained using

$$\mathbf{H}_{\mathrm{d}}(\mathbf{r}_i) = -\nabla\phi_{\mathrm{M}}(\mathbf{r}_i) \tag{A16}$$

from potential theory. Numerically, this gradient was estimated with a centered difference of the nearest-neighbor sites, except on the boundaries, where forward or backward differencing was used. Note that the discretizations of all operators have been chosen for consistency between surface and volume charges such that the model magnet can be padded by volumes of lattice sites with $\mathbf{M}=0$ without changing the results.

The FMM was implemented using C++ and named Hierarchy.h. Fundamental to the implementation is the class sh_expansion whose instances are a $(p+1)^2$ array of complex numbers representing either local or multipole expansion coefficients. The class includes methods for indexing expansion coefficients within an expansion, evaluating the expansion at a specified point, and transforming an expansion using Eqs. (A7), (A10), and (A12). In addition, the class encapsulates the precomputation of quantities that do not depend on the displacement vector, and it can return a pointer to a table of precomputations that do depend on a fixed displacement. For instance, for efficient evaluation of the translation of multipole expansions, Eq. (A7), the class contains the $(p+1)^4$ values

$$C^{j,l}_{i,k}=\frac{J^{j-l}_{l}A^{l}_{k}A^{j-l}_{i-k}}{A^{j}_{i}} \tag{A17}$$

and an indirect-indexing array that specifies the sequence of $O_{k,l}$ after the loops have been unrolled. In addition, a pointer to the $(p+1)^2$ precomputed values of $\varrho^k Y^{-l}_k(\theta,\varphi)$ can also be returned. Thus the transformation can be evaluated efficiently and with minimal overhead from loop-control variables.

The computer memory requirements to store the precomputations that depend on spatial relationships can be greatly reduced for implementations that assume a regular lattice for spatial decomposition. For each level of the hierarchy, there will be a fixed number of displacements between the cells in that level and with cells on the parent level and the child level. The class sh_expansion encapsulates this efficiency at each request for a precomputation by searching a linked list of previous results and creating a new result only when no previous result exists. A similar scheme is also necessary for the compilation of multipole expansion coefficients for the lowest level of the hierarchy, Eq. (A6). Since the precomputations represent a significant amount of the memory requirements of the overall simulation, these memory savings can greatly increase the number of lattice points used to represent the model magnet.

The partitioning of space is accomplished through the class hbox. Instances of this class contain geometric information about the decomposition cell and expansions for both the potential and charges within the cell, as well as links to other cells. These links point to the encompassing cell, the encompassed cells, a list of same-level cells in the far field (the "interacting cells"), and a list of nearest-neighbor cells. The hbox's for each level of the decomposition hierarchy are held in a container class hlevel, and the entire hierarchy is maintained as a linked list. Our implementation of hlevel is particular to the cubic-lattice decomposition of space, and irregular geometries have to be padded with empty space. (This is also true for our implementation of the classes VectorField and ScalarField from VectorField.h used throughout our numerical integration of the LLG equation.)

APPENDIX B

A useful way to represent the thermal Landau-Lifshitz-Gilbert equation is in a form with the deterministic and stochastic parts separated

$$\begin{aligned} d\mathbf{M}(\mathbf{r}_i,t)=&\,\mathbf{B}[\mathbf{M}(\mathbf{r}_i,t)]\mathbf{H}_{\mathrm{det}}(\mathbf{r}_i,t)dt\\ &+\sqrt{\epsilon}\,\mathbf{B}[\mathbf{M}(\mathbf{r}_i,t)]d\mathbf{W}(\mathbf{r}_i,t), \end{aligned} \tag{B1}$$

where $\mathbf{H}_{\mathrm{det}}(\mathbf{r}_i,t)$ is the deterministic part of the local field at $\mathbf{r}_i$ and $\mathbf{H}_n(\mathbf{r}_i)=\sqrt{\epsilon}d\mathbf{W}(\mathbf{r}_i,t)$ is the stochastic part. The matrix $\mathbf{B}$ is given by

$$\mathbf{B}[\mathbf{M}(\mathbf{r}_i,t)]=\frac{1}{1+\alpha^2}\begin{pmatrix} \alpha(M_y^2+M_z^2) & -M_z-\alpha M_xM_y & M_y-\alpha M_xM_z\\ M_z-\alpha M_xM_y & \alpha(M_x^2+M_z^2) & -M_x-\alpha M_yM_z\\ -M_y-\alpha M_xM_z & M_x-\alpha M_yM_z & \alpha(M_x^2+M_y^2) \end{pmatrix}, \tag{B2}$$

where *x*, *y*, and *z* represent the Cartesian coordinates and the space and time dependences of the M_μ have been omitted for clarity. The stochastic nature of the field results from the Wiener[34–36] process $\mathbf{W}(\mathbf{r}_i,t)$ which has the properties

$$\begin{aligned} &\langle W_\mu(\mathbf{r}_i,t)\rangle=0,\\ &\langle W_\mu(\mathbf{r}_i,t)W_{\mu'}(\mathbf{r}'_i,t')\rangle=(t-t')\,\delta_{\mu,\mu'}\delta_{i,i'}\,. \end{aligned} \tag{B3}$$

The stochastic differential equation (B1) can be treated numerically using first-order Euler integration. For small Δt, the deterministic integral is

$$\mathbf{I}_{\mathrm{det}}(\mathbf{r}_i,t)=\mathbf{B}[\mathbf{M}(\mathbf{r}_i,t)]\mathbf{H}_{\mathrm{det}}(\mathbf{r}_i,t)\Delta t. \tag{B4}$$

The integral of the stochastic part,

$$\mathbf{I}_{\mathrm{sto}}(\mathbf{r}_i,t)=\sqrt{\epsilon}\int_t^{t+\Delta t}\mathbf{B}[\mathbf{M}(\mathbf{r}_i,t')]d\mathbf{W}(\mathbf{r}_i,t'), \tag{B5}$$

takes more consideration since it involves the product of the magnetization with the Wiener process. In such cases of multiplicative noise, different methods for evaluating Eq. (B5) correspond to different Fokker-Planck equations.[34–37] There are an infinite number of ways to interpret Eq. (B5), but usually only the two extreme cases, the Itô and Stratonovich interpretations, are considered. The Fokker-Planck equation considered by Brown[9] only has the proper equilibrium properties when interpreted in the Stratonovich sense.[2] This is complicated by the fact that numerical implementation of the stochastic integral is particularly convenient in the Itô interpretation. Then the discretized integral is[38]

$$\mathbf{I}_{\mathrm{sto}}(\mathbf{r}_i,t)=\sqrt{\epsilon\,\Delta t}\,\mathbf{B}[\mathbf{M}(\mathbf{r}_i,t)]\mathbf{g}(\mathbf{r}_i,t), \tag{B6}$$

where each component of $\mathbf{g}$ is a random number from a Gaussian distribution with zero mean and unit variance. Fortunately, changing interpretations can be accomplished through a correction discussed below. Then, Eq. (B6) can be combined with Eq. (B4), and the result rearranged, to give the "impulse" during the integration step, Eq. (11).) Changing from the Stratonovich interpretation of the stochastic integral to that of Itô requires the addition of a deterministic term. Specifically, a Stratonovich interpretation of a multivariate-Langevin equation of the form

$$d\mathbf{x} = \mathbf{a}(\mathbf{x},t)\,dt + \mathbf{b}(\mathbf{x},t)\,d\mathbf{W} \tag{B7}$$

is equivalent to the Langevin equation[34]

$$d\mathbf{x} = [\mathbf{a}(\mathbf{x},t) + \mathbf{c}(\mathbf{x},t)]\,dt + \mathbf{b}(\mathbf{x},t)\,d\mathbf{W} \tag{B8}$$

in the Itô interpretation[34,36] where the components of the new drift term are

$$c_\mu = \frac{1}{2} \sum_{\nu,\nu'} b_{\nu',\nu} \frac{\partial b_{\mu,\nu}}{\partial \nu'}. \tag{B9}$$

For the present system, the additional drift term is readily found to be

$$\mathbf{c}(\mathbf{r}_i,t) = \frac{\epsilon}{(1+\alpha^2)} \mathbf{M}(\mathbf{r}_i,t), \tag{B10}$$

which is equivalent to the result given in Ref. 2. This drift term is always directed along the local magnetization density. The process of normalizing the magnitude of the spins during each integration step, Eq. (10), is also directed along the magnetization and, essentially, takes the correction into account.

---

[1] J.J.M. Ruigrok, R. Coehoorn, S.R. Cumpson, and H.W. Kesteren, J. Appl. Phys. **87**, 5398 (2000).

[2] J.L. García-Palacios and F.J. Lázaro, Phys. Rev. B **58**, 14 937 (1998).

[3] G. Brown, M.A. Novotny, and P.A. Rikvold, J. Appl. Phys. **87**, 4792 (2000).

[4] G. Brown, M. A. Novotny, and P.A. Rikvold, in *Magnetic Storage Systems Beyond 2000*, edited by G. Hadjipanayis (Kluwer, Dordrecht, in press).

[5] G. Brown, M.A. Novotny, and P.A. Rikvold, J. Appl. Phys. **89**, 7588 (2001).

[6] D.A. Garanin, Phys. Rev. B **55**, 3050 (1997).

[7] W.F. Brown, *Micromagnetics* (Wiley, New York, 1963).

[8] A. Aharoni, *Introduction to the Theory of Ferromagnetism* (Clarendon, Oxford, 1996).

[9] W.F. Brown, Phys. Rev. **130**, 1677 (1963).

[10] B.D. Cullity, *Introduction to Magnetic Materials* (Addison-Wesley, Reading, MA, 1972).

[11] S. Wirth, M. Field, D.D. Awschalom, and S. von Molnár, Phys. Rev. B **57**, R14 028 (1998).

[12] The value of the exchange length used, $l_\mathrm{e} = 3.6$ nm, here has been adjusted to account for a multiplicative factor of 2 that we initially believed should appear in Eq. (3); see Ref. 29. A more common value for iron is $l_e = 2.6$ nm (see Refs. 10 and 11), which is approximately $1/\sqrt{2}$ times the value used here.

[13] X.B. Feng and P.B. Visscher, J. Appl. Phys. **89**, 6988 (2001).

[14] U. Nowak, R.W. Chantrell, and E.C. Kennedy, Phys. Rev. Lett. **84**, 163 (2000).

[15] U. Nowak, in *Annual Reviews of Computational Physics IX*, edited by D. Stauffer (World Scientific, Singapore, 2001), p. 105.

[16] A.S. Arrot, B. Heinrich, and D.S. Bloomberg, IEEE Trans. Magn. **MAG-10**, 950 (1974).

[17] L.F. Greengard, *The Rapid Evaluation of Potential Fields in Particle Systems* (MIT Press, Cambridge, 1988).

[18] V.L. Safanov and T. Suzuki, IEEE Trans. Magn. **MAG-34**, 1860 (1998).

[19] S. Wirth, M. Field, D.D. Awschalom, and S. von Molnár, J. Appl. Phys. **85**, 5249 (1999).

[20] D. Hinzke and U. Nowak, Comput. Phys. Commun. **122**, 334 (1999).

[21] U. Nowak and D. Hinzke, J. Appl. Phys. **85**, 4337 (1999).

[22] H.N. Bertram and C. Seberino, J. Magn. Magn. Mater. **193**, 388 (1999).

[23] Y.D. Yan and E. Della Torre, J. Appl. Phys. **66**, 320 (1989).

[24] S.T. Chui and D.-C. Tian, J. Appl. Phys. **78**, 3965 (1995).

[25] K.J. Kirk, J.N. Chapman, and C.D.W. Wilkinson, Appl. Phys. Lett. **71**, 539 (1997).

[26] T.-N. Fang and J.-G. Zhu, J. Appl. Phys. **87**, 7061 (2000).

[27] N. Dao, S.R. Homer, and S.L. Whittenburg, J. Appl. Phys. **86**, 3262 (1999).

[28] R.H. Koch, G. Grinstein, G.A. Keefe, Y. Lu, P.L. Trouilloud, W.J. Gallagher, and S.S.P. Parkin, Phys. Rev. Lett. **84**, 5419 (2000).

[29] E.D. Boerner and H.N. Bertram, IEEE Trans. Magn. **MAG-33**, 3052 (1997).

[30] R.E. Dunin-Borkowski, M.R. McCartney, B. Kardynal, D.J. Smith, and M.R. Scheinfein, Appl. Phys. Lett. **75**, 2641 (1999).

[31] R.P. Cowburn and M.E. Welland, Science **287**, 1466 (2000).

[32] K. Ramstöck, T. Leibl, and A. Hubert, J. Magn. Magn. Mater. **135**, 97 (1994).

[33] J.D. Jackson, *Classical Electrodynamics*, 2nd ed. (Wiley, New York, 1975), Eq. (5.100).

[34] C.W. Gardiner, *Handbook of Stochastic Methods*, 2nd ed. (Springer, Berlin, 1985).

[35] N.G. van Kampen, J. Stat. Phys. **24**, 175 (1981).

[36] N.G. van Kampen, *Stochastic Processes in Physics and Chemistry* (Elsevier, Amsterdam, 1992).

[37] M. San Miguel and R. Toral, in *Instabilities and Nonequilibrium Structures V*, edited by E. Tirapegui and W. Zeller (Kluwer, Dordrecht, 1999).

[38] J.R. Klauder and W.P. Petersen, SIAM (Soc. Ind. Appl. Math.) J. Numer. Anal. **22**, 1153 (1985).